# Bipolar switching by HCN voltage sensor underlies hyperpolarization activation

John Cowgill[a], Vadim A. Klenchin[a], Claudia Alvarez-Baron[a], Debanjan Tewari[a], Alexander Blair[a], and Baron Chanda[a,b,1]

[a]Department of Neuroscience, University of Wisconsin–Madison, Madison, WI 53705; and [b]Department of Biomolecular Chemistry, University of Wisconsin–Madison, Madison, WI 53706

Edited by Richard W. Aldrich, The University of Texas at Austin, Austin, TX, and approved November 26, 2018 (received for review September 27, 2018)

**Despite sharing a common architecture with archetypal voltage-gated ion channels (VGICs), hyperpolarization- and cAMP-activated ion (HCN) channels open upon hyperpolarization rather than depolarization. The basic motions of the voltage sensor and pore gates are conserved, implying that these domains are inversely coupled in HCN channels. Using structure-guided protein engineering, we systematically assembled an array of mosaic channels that display the full complement of voltage-activation phenotypes observed in the VGIC superfamily. Our studies reveal that the voltage sensor of the HCN channel has an intrinsic ability to drive pore opening in either direction and that the extra length of the HCN S4 is not the primary determinant for hyperpolarization activation. Tight interactions at the HCN voltage sensor–pore interface drive the channel into an hERG-like inactivated state, thereby obscuring its opening upon depolarization. This structural element in synergy with the HCN cyclic nucleotide-binding domain and specific interactions near the pore gate biases the channel toward hyperpolarization-dependent opening. Our findings reveal an unexpected common principle underpinning voltage gating in the VGIC superfamily and identify the essential determinants of gating polarity.**

ion channel | HCN | hyperpolarization | EAG | depolarization

A salient feature of a living cell is that its resting membrane potential is more negative inside than outside. Electrical signaling is mediated by voltage-gated ion channels which are activated by membrane depolarization in response to a variety of stimuli (1, 2). However, a subclass of voltage-gated channels is activated when the membrane potential is made more negative (3, 4). These hyperpolarization-activated and cyclic nucleotide-gated (HCN) channels drive the membrane potential toward threshold in autonomously rhythmic cells such as the sinoatrial node, and are also known as pacemaking channels (5).

HCN channels belong to the cyclic nucleotide-binding domain (CNBD) clade of the voltage-gated ion channel (VGIC) superfamily, which also includes depolarization-activated EAG (ether-à-go go) and hERG (human ether-à-go go related) channels (6–8). Although the hERG channel is depolarization-activated, it behaves in some ways like a hyperpolarization-activated ion channel (9, 10). Their depolarization-dependent opening is obscured by rapid inactivation but, upon repolarization, they pass large "resurgent" currents, because the channels returning from the inactivated state are slow to close (9, 11, 12). In contrast to hERG, HCN channels do not exhibit resurgent currents, and there is no evidence that the wild-type HCN opens at depolarized potentials.

However, similar to depolarization-activated channels, HCN channels utilize positive charges on the S4 helix to sense voltage (13) and an intracellular gate to regulate ion conduction (14–16). Therefore, the prevailing hypothesis has been that it is simply an inversion of coupling between the two domains that accounts for the inversion of gating in the HCN channel. Nevertheless, later cysteine accessibility studies suggest that the voltage sensor of HCN1 undergoes a noncanonical conformational change upon hyperpolarization (17, 18). The recent cryo-EM structures of HCN (19) and EAG (20) show that, despite some differences, their overall architecture is remarkably similar. These structures also imply that there must be subtle molecular-level interactions that ultimately control the gating polarity in the CNBD family.

To identify the essential molecular determinants of gating polarity in EAG and HCN channels, we used a top-down protein-engineering approach. First, we identified the portable structural modules in these channels, and then tested the role of these modules in channel function by making swaps. Although such horizontal swaps have been remarkably successful in identifying self-contained catalytic or functional sites, they do not reconstruct allosteric interaction pathways involved in signal transduction between the structural modules. Therefore, in the next round, we introduced specific interactions that are likely to be involved in coupling the voltage sensor and pore gates to create "mosaic" channels. Our studies reveal that the voltage-sensing domain of HCN channels is a bipolar switch that can drive the pore opening in both the hyperpolarized and depolarized direction. In the HCN, the opening at depolarized potentials is abrogated by rapid inactivation upon depolarization due to the tight S4–S5 interface. Other structural elements including key residues near the gate and the C-terminal cytoplasmic region stabilize the opening at hyperpolarized potentials. Taken together, our studies reveal a unifying mechanistic thread that links the distinct voltage-dependent gating phenotypes exhibited by channels in this superfamily.

## Results

**Voltage-Sensing Segment of HCN Can Drive Opening During Both Hyperpolarization and Depolarization.** Despite major differences in function, the overall architectures of HCN1 and EAG1 are

### Significance

Hyperpolarization-activated, cyclic nucleotide-gated (HCN) channels show an inverted voltage response compared with virtually all other voltage-gated channels, opening on hyperpolarization rather than depolarization. Although the structure of the HCN1 channel was recently solved, the structural element(s) responsible for the inverted gating polarity of HCN is not known. Here, we use a hierarchical approach, by first characterizing the functional contribution of each structural element to channel gating, and then identifying the critical interactions between these elements. Our studies reveal that the HCN voltage sensor can gate the same pore open on both depolarization and hyperpolarization, thereby acting as a bipolar switch. Elements in the pore domain shut off the depolarization-activation pathway in wild-type channels.

Author contributions: J.C., V.A.K., C.A.-B., and B.C. designed research; J.C., V.A.K., C.A.-B., D.T., and A.B. performed research; B.C. contributed new reagents/analytic tools; J.C., C.A.-B., D.T., and A.B. analyzed data; and J.C., V.A.K., and B.C. wrote the paper.

The authors declare no conflict of interest.

This article is a PNAS Direct Submission.



[1]To whom correspondence should be addressed. Email: chanda@wisc.edu.

This article contains supporting information online at www.pnas.org/lookup/suppl/doi:10.1073/pnas.1816724116/-/DCSupplemental.

Published online December 26, 2018.

remarkably similar (Fig. 1*A*) (19, 20). Detailed examination reveals that several structural elements including the gating scaffold (S1–S3a), voltage sensor (S3b–S4), pore module (S5–S6), and cytoplasmic C-terminal region are highly conserved (Fig. 1*B*). Nevertheless, there are key differences between HCN channels and depolarization-activated members of potassium voltage-gated channel subfamily H (KCNH). HCN channels contain an N-terminal HCN-specific domain in place of the PAS domain found in the KCNH channels (21, 22), and their S4 transmembrane helix is at least two helical turns longer than its counterpart in the EAG1 and hERG (19).

To test the role of each of these structural elements, we created chimeras by swapping elements between the inward- and outward-rectifying channels. Previous studies have identified modular elements in VGICs such as the pore domain (23), voltage-sensing domain (24), and voltage-sensing paddle (25), but the junction points for making such swaps have not been identified in HCN channels. With the aid of the recent high-resolution structures (19, 20), we first performed sequence alignment between the HCN homologs (mHCN1, mHCN2, and spHCN, where the m-prefix denotes the mouse orthologs and the sp-prefix denotes the homolog from *Strongylocentrotus purpuratus*) and EAG1 channels (*SI Appendix*, Fig. S1) to identify junction points for making these swaps. This structure-based sequence alignment allowed us to identify the regions which despite differences in primary sequence have a similar 3D structure. These sites were used to create chimeras although, in some instances, multiple chimeras with different junction points were tested (*SI Appendix*, Fig. S2). Based on this preliminary scan, we empirically identified four primary junction points that demarcate

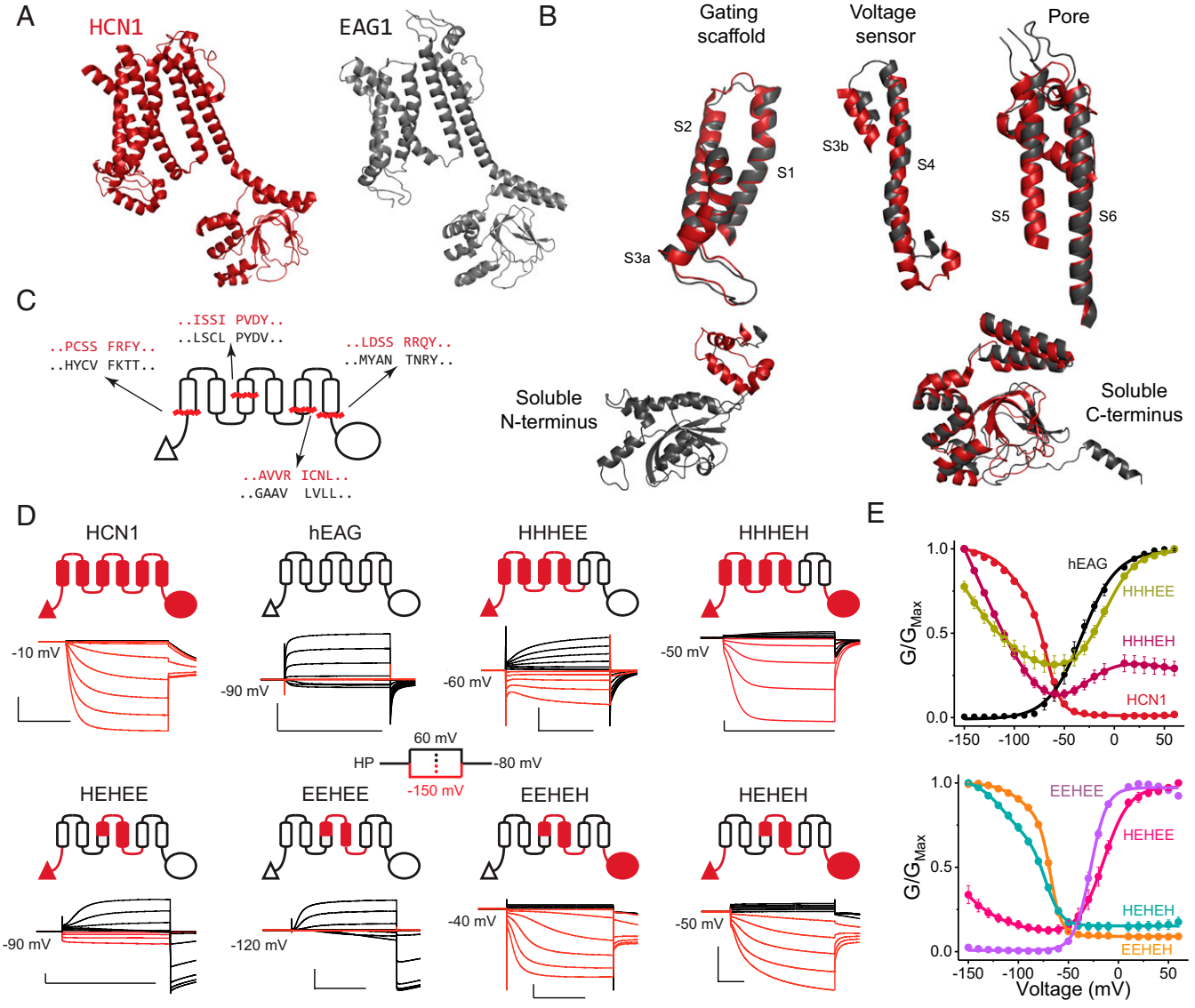


**Fig. 1.** HCN voltage-sensing domain is a bipolar switch. (*A*) Monomeric structures of hHCN1 and rEAG1 (the r-prefix denotes the rat homolog). The color coding for HCN1 (red) and EAG1 (black) is used throughout all figure panels. The N terminus of rEAG1 is omitted for clarity. (*B*) Structural alignment between hHCN1 and rEAG1 for the five modular segments used in generating the chimeric channels. (*C*) Cartoon representation showing the local sequence alignments of mHCN1 and hEAG1 around the junction points used in generating chimeric channels. (*D*) Cartoon representations of chimeric channels and representative traces for currents elicited in cut-open voltage clamp under symmetrical solutions (100 mM $K^+_{internal}$/100 mM $K^+_{external}$). Currents in response to depolarizing pulses are colored black, and responses to hyperpolarizing pulses are colored red for clarity. [Scale bars, 2 μA (vertical) and 500 ms (horizontal).] (*E*) Conductance–voltage curves for the parent and chimeric channels. Error bars are SEM from $n = 5$ (HHHEH and EEHEE), 6 (HEHEH), or 4 (all others) independent measurements.

five structural elements common to these channels (Fig. 1*C*). Henceforth, we will denote these chimeras using a five-letter code representing the origin of each structural element: H for mHCN1 and E for hEAG.

Given the modularity of the voltage-sensing and pore domains (23, 26), we first tested the HHHEE chimera that contains the voltage-sensing domain of HCN1 and pore domain of EAG1 (Fig. 1 *D* and *E*). Remarkably, this chimera opens in a voltage-dependent manner both at hyperpolarizing and depolarizing potentials while closing at intermediate potentials (HHHEE in Fig. 1*D*). This behavior, which we refer to as the bipolar phenotype, establishes that the hyperpolarization- and depolarization-activation pathways are distinct and that the HCN voltage-sensing domain is intrinsically capable of gating the pore in both directions. Swapping the soluble C-terminal region of the HCN channel into this chimera (HHHEH) maintains the basic phenotype but reduces the depolarization-activated currents. Together, these results suggest that the C terminus of HCN contributes to shutting the depolarization-activated pathway.

The voltage-sensing domain has three structural elements: the N-terminal HCN domain (19), gating scaffold, and voltage-sensor paddle. Replacement of the gating scaffold in the HHHEE chimera with its equivalent from EAG1 (HEHEE) results in a channel which primarily activates upon depolarization, although these channels can still open upon hyperpolarization. Further replacement of the N terminus with that of EAG1 (EEHEE chimera) completely abolishes activation by hyperpolarization, and this construct behaves like a canonical outward-rectifying channel (Fig. 1 *D* and *E*). These findings establish that the HCN S4 paddle is not sufficient to drive the channels to open upon hyperpolarization, and that it requires cumulative contribution from both the gating scaffold and N terminus to stabilize the hyperpolarization-activated opening.

The role of the HCN C terminus was further examined by generating two other chimeras, EEHEH and HEHEH. Surprisingly, these chimeras show activation upon hyperpolarization but very little activation on depolarization (compare with the EAG-like EEHEE and HEHEE; Fig. 1*E*). Thus, unlike the N terminus, which enhances hyperpolarization activation without perturbing the depolarization-activation pathway, the C terminus of HCN appears to disfavor activation upon depolarization in addition to enhancing opening at hyperpolarized potentials. Nevertheless, both EEHEH and HEHEH also exhibit substantial voltage-independent leak conductance (~10% of the maximum), indicating that these channels are still missing some elements required for full closure at depolarized potentials.

**Hyperpolarization- and Depolarization-Activated States Share the Same Permeation Pathway.** Although currents observed from oocytes expressing the chimeras are much larger and distinct in appearance from endogenous currents of uninjected oocytes (*SI Appendix*, Fig. S3), it is important to rule out the possibility that these are simply up-regulated or altered endogenous conductances, as has been observed previously (27). Additionally, subtle perturbations within the voltage-sensing domain have been shown to create additional ion-permeation pathways through the voltage-sensing domain. These gating-pore currents are distinct from the central-pore currents (28–30) and, in many cases, they are elicited upon hyperpolarization. To probe the source and permeation pathway of the elicited currents, we introduced a cysteine residue near the selectivity filter (hEAG1 mutant A470C; Fig. 2*A*) and evaluated the effect of methanethiosulfonate ethylammonium (MTSEA) modification on ionic currents. The A470C mutants of EAG1 and HHHEH show ~60% reduction in current amplitude upon addition of MTSEA, whereas the parent constructs are unaffected (Fig. 2 *B* and *C*). Importantly, currents at both hyperpolarizing and depolarizing potentials are inhibited by cysteine modification and persist even after a 30-s washout (*SI Appendix*, Fig. S3). These findings establish that the observed conductances

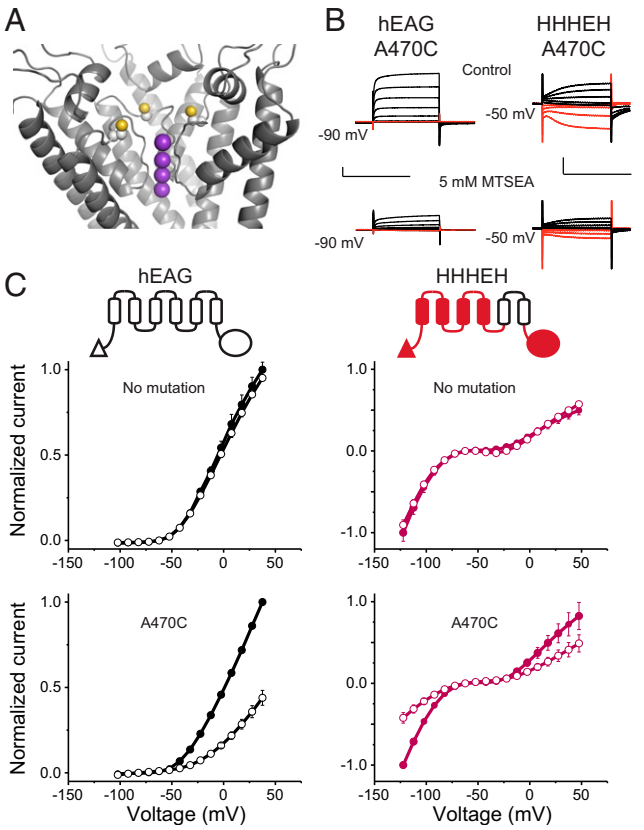


**Fig. 2.** Hyperpolarization- and depolarization-activated states share the same permeation pathway. (*A*) Location of the A470C mutation near the selectivity filter in the rEAG1 structure (yellow balls indicate sulfur atoms). Only three subunits are shown for clarity. Purple balls indicate positions of potassium ions as would be expected for EAG1 based on experimentally determined sites in the similar selectivity filter of Kv1.2/2.1. (*B*) Representative current traces for A470C mutants of EAG1 and HHHEH from two-electrode voltage clamp. Currents from EAG1-A470C were recorded in 100 mM $Na^+$/5 mM $K^+$, while the HHHEH-A470C was recorded under pseudosymmetric conditions using the same external solution as in Fig. 1. (*B*, *Top*) Traces represent initial recordings. (*B*, *Bottom*) Traces represent recordings following application of 5 mM MTSEA shown on the same scale. [Scale bars, 2 μA (vertical) and 500 ms (horizontal).] (*C*) Normalized current–voltage relationships for EAG (*Left Top*), HHHEH (*Right Top*), hEAG-A470C (*Left Bottom*), and HHHEH-A470C (*Right Bottom*) channels before (filled circles) and after (open circles) MTSEA addition, with error bars showing SEM for $n = 2$ (HHHEH), 3 (EAG1), 6 (EAG1-A470C), or 8 (HHHEH-A470C).

at both potentials are due to ion flux through the central pore of the expressed channels.

**HCN1-Like S4–S5 Interface Introduces a Rapid Inactivation Pathway on Depolarization.** One of the most striking features of the HCN1 structure is the tight juxtaposition of the S4 and S5 helices in contrast to the depolarization-activated channels like EAG and Kv1.2/2.1 (19, 20, 31). To test the hypothesis that this unique hairpin-like structure formed by the S4 and S5 helices of HCN1 contributes to the inverted polarity, we sought to reconstruct the S4–S5 interface in our chimeras by mutating the six S4-facing residues on the S5 helix of EAG1 to the HCN1 equivalents (Fig. 3*A*). We refer to these constructs as mosaics, and henceforth they will be denoted with an asterisk.

The introduction of the mosaic mutations into the HHHEE, HHHEH, and EEHEH chimeras resulted in a near-complete loss of conductance at depolarizing potentials (Fig. 3 *B* and *C*). More significantly, we observed prominent tail currents upon repolarization despite the lack of currents on depolarization in

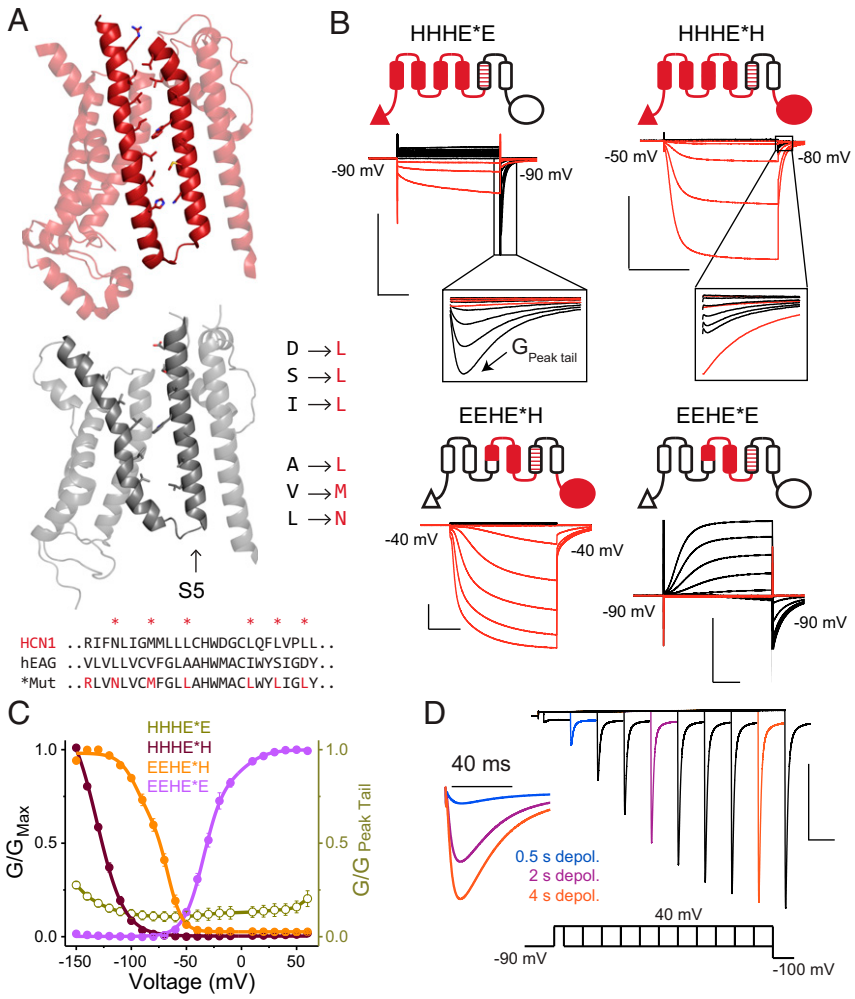


**Fig. 3.** HCN1-like S4–S5 interface induces rapid inactivation upon depolarization. (*A*) Structures of the transmembrane regions of hHCN1 (*Top*) and rEAG1 (*Middle*) highlighting the S4–S5 interface. The sequence alignment indicates the S5 residues of the EAG1 pore that were mutated to their HCN1 equivalents to preserve S4–S5 interfacial interactions. (*B*) Cartoon representations of the mosaic chimeras and representative COVG current traces in symmetrical solutions (100 mM $K^+_{in}$/100 mM $K^+_{ex}$). Mosaic mutations are designated with an asterisk in the construct name. (*B*, *Insets*) Expanded view of tail currents displaying the hooked phenotype. (*C*) Steady-state G-V curves for mosaic channels depicted in *B*, with error bars representing SEM for $n = 3$ (HHHE*E and EEHE*H) or 4 (for all others). In the HHHE*E construct, the maximum conductance was observed in the tails upon repolarization to the indicated potentials. Therefore, the steady-state conductances were normalized to the maximum tail current (labeled as $G_{Peak\ tail}$ in *B*). The data points for HHHE*E are thus plotted as open symbols using a separate axis (*Right*) to emphasize this difference. This convention is used to highlight the fact that only a small fraction of channels are open at steady state. (*D*) Envelope-of-tails experimental protocol used with the HHHE*E construct to evaluate tail currents elicited by depolarizing +40-mV pulses of varying duration. Three traces for 0.5-, 2-, and 4-ms pulses are colored and reproduced at higher temporal resolution (*Left*). [Scale bars, 2 μA (vertical) and 500 ms (horizontal).]

both the HHHE*E and HHHE*H mosaics (Fig. 3*B*). These tail currents are characterized by an unusual "hooked" phenotype which is observed when channels inactivate rapidly upon opening. For noninactivating channels like EAG, its tail currents upon return to negative potentials decay exponentially to baseline as the channel closes. However, if the channel enters an inactivated state after opening, its tail current is biphasic. The rising phase of the current corresponds to recovery from inactivation and entry into the open state, whereas the subsequent falling phase represents closing of these channels at those potentials. These currents are referred to as hooked tails. However, in the case of the HHHE*E and HHHE*H mosaics, the hooked-tail currents are much more robust even in comparison with the depolarization-activated currents. These currents are referred to as resurgent tail currents, and are observed when the rate of entry into the inactivated state is much faster than the rate of channel opening (see simulations in *SI Appendix*, Fig. S4). In such instances, channel opening upon depolarization is obscured by inactivation, resulting in small currents at those potentials. In contrast, upon returning from depolarization, the channels recover rapidly from inactivation but are slow to close, resulting in large resurgent-tail currents. This behavior is characteristic of the hERG potassium channel, which is involved in repolarization of cardiac action potentials (9, 11). Note that resurgent-tail currents by definition are hooked, whereas hooked tails need not be resurgent.

To test whether the lack of currents on depolarization is due to an hERG-like gating scheme, we used envelope-of-tails and three-pulse protocols for HHHE*E, assessing the kinetics of activation and inactivation, respectively (11, 12). The envelope-of-tails protocol shows that the amplitudes of peak tail current increase over many seconds with depolarizations of increased length, although there is no increase in steady-state currents (Fig. 3*C* and *SI Appendix*, Fig. S4). Furthermore, a three-pulse protocol probing the entry into the inactivated state shows that the open channel inactivates over several milliseconds at depolarized potentials. These results show that the S4–S5 interface of

HCN1 plays a critical role in preventing conduction at depolarized potentials through a rapid inactivation process. However, while hERG inactivation can be slowed by the presence of external tetraethylammonium ($TEA^+$) (12), the inactivation of the HHHE*E mosaic is unaffected by external $TEA^+$ (*SI Appendix*, Fig. S4). These findings suggest that while the inactivation of the HHHE*E mosaic is phenomenologically similar to hERG, the underlying molecular mechanism may be quite distinct (32).

Although addition of HCN S4–S5 interfacial residues reduced the conductance at depolarized potentials for most mosaics, this was not the case for the EEHE*E construct (Fig. 3 *B* and *C*). This behavior is not surprising, because deletions of the soluble N-terminal PAS domain of EAG1 (33, 34) and chimera experiments (35) have shown that interactions between the PAS domain and C-terminal cyclic nucleotide-binding homology domain are necessary to prevent voltage-dependent inactivation in EAG channels.

**Role of HCN1 C Terminus in Regulating Polarity of Voltage-Dependent Gating.** Our data thus far suggest that the C terminus plays a critical role in regulating the polarity of voltage gating. Replacing the EAG1 C terminus with its HCN1 counterpart in either the HHHEE or EEHEE chimera leads to a substantial increase in activation by hyperpolarization. Given that voltage-dependent activation of HCN1 is virtually unaffected by removal of its C terminus (36) (see also *SI Appendix*, Fig. S5), we speculated that the removal of the EAG1 C terminus, rather than addition of the HCN1 equivalent, may account for these observations. However, removal of the C-terminal cytoplasmic region from the HHHE*E mosaic increases currents upon depolarization relative to hyperpolarization (Fig. 4 *A* and *B*). Therefore, we conclude that the HCN C-terminal cytoplasmic domain directly prevents channel opening upon depolarization while also stabilizing channel opening upon hyperpolarization.

The C-terminal cytoplasmic domain of the HCN channel can be subdivided into two functional and structural elements (37–39): the CNBD that directly binds to the cyclic nucleotides, and the C-linker domain that links the CNBD to the pore helices. The structure shows that the CNBD interacts with the rest of the channel allosterically through the C linker, which directly interacts with the voltage-sensing and pore domains. To evaluate whether direct interactions between the C linker and the voltage sensor or pore can account for the phenotypic effect of the C terminus, we tested a deletion construct lacking the CNBD (HHHE*H-ΔCNBD). Although, compared with the C-terminal deletion, the ΔCNBD construct slightly increases currents upon hyperpolarization, it is unable to significantly destabilize the opening at depolarized potentials (Fig. 4 *A* and *B*). Thus, the intact C terminus which includes both the CNBD and the C linker is required for the robust inverted gating phenotype observed in the HHHE*H mosaic.

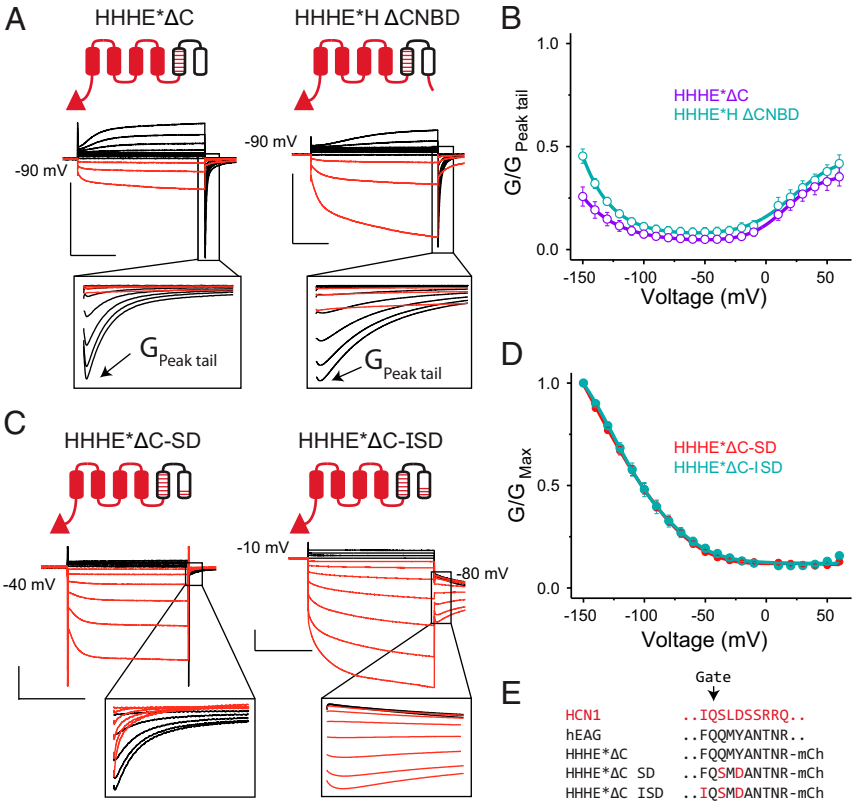


**Fig. 4.** Role of HCN1 C terminus and residues near the gate in regulating gating polarity. (*A*) Cartoons and representative COVG currents for truncation constructs that lack either the entire cytoplasmic C terminus (HHHE*ΔC) or CNBD (HHHE*H-ΔCNBD; residues following S478 of mHCN1 are removed from HHHE*H). (*A*, *Insets*) Expanded views of the tail currents to show the kinetic features more clearly. [Scale bars, 2 μA (vertical) 500 ms (horizontal) in all panels.] Tail pulse is at the holding potential. (*B*) G-V curves for the C-terminal truncations depicted in *A*, with error bars representing SEM for $n = 3$. For the same reasons noted in Fig. 3*C* for the HHHE*E construct, the steady-state conductance for both these truncations was normalized to their respective maximum tail currents. (*C*) Cartoons and representative COVG currents for the double and triple mutants of HHHE*ΔC. Note the *Insets* that show that the HHHE*ΔC-SD construct still exhibits hooked-tail currents on depolarizing pulses, while HHHE*ΔC-ISD does not. Tail pulse is at the holding potential unless noted otherwise. (*D*) G-V curves for the HHHE*ΔC-SD and HHHE*ΔC-ISD channels, with error bars showing SEM for $n = 4$ (HHHE*ΔC-SD) or 9 (HHHE*ΔC-ISD). (*E*) Sequences near the channel's main gate in the S6 helix for mHCN1, hEAG1, HHHE*ΔC, and additional mutants made in the HHHE*ΔC background.

**Residues at the Tail of S6 Helix Destabilize the Depolarization-Activated Open State.** Although the C-terminal cytoplasmic domain is essential for the inverted gating phenotype in the chimeras, wild-type HCN channels lacking this region gate open upon hyperpolarization (36) (see also *SI Appendix*, Fig. S5). Further, the HHHE*H mosaic displays resurgent currents upon return from depolarization, which are not observed in HCN1. Therefore, elements within the HCN pore domain (S5–S6) must contribute to the inverted gating polarity and lack of resurgent currents in HCN1. By testing a series of constructs on the HHHE*H background in which an increasingly larger proportion of the pore domain is replaced by HCN1-specific residues, we were able to completely suppress resurgent currents by swapping out the last six residues of S6 (*SI Appendix*, Fig. S6). To test whether these six residues on the S6 helix of HCN contribute to channel gating independent of the C terminus, we substituted these residues into the HHHE*ΔC mosaic. The resultant mosaic (HHHE*ΔC2) is primarily activated upon hyperpolarization, though resurgent-tail currents are still observed upon return from depolarization (*SI Appendix*, Fig. S6). This shows that these terminal S6 residues are critical for inverting the gating polarity by preventing opening at depolarized potentials.

Alanine-scanning mutagenesis in this region has previously shown that the two conserved S6 residues S441 and D443 in mHCN2 stabilize the closed state at depolarizing potentials (40). Just replacing these two residues in the HHHE*ΔC parent recapitulates the gating phenotype of the six-residue swap (HHHE*ΔC-SD in Fig. 4 *C*–*E*). While substitution of these two residues prevents opening upon depolarization and leads to an inverted gating polarity similar to HCN1, robust resurgent currents are still observed upon return from depolarization, unlike HCN1ΔC constructs (*SI Appendix*, Fig. S6). Examination of the rEAG1 structure reveals that an aromatic residue, F475, immediately preceding the gate may be involved in pi-stacking interactions with Y479. The equivalent residue in all HCN-like channels is a highly conserved isoleucine. Substituting this isoleucine into the HHHE*ΔC-SD construct completely abolishes the resurgent-tail currents (HHHE*ΔC-ISD in Fig. 4*C*). In summary, these three HCN pore residues are able to functionally replace the entire cytoplasmic C-terminal domain.

**Long S4 Helix Is Not Required for Activation by Hyperpolarization.** Thus far, all of our chimeras and mosaics that open upon hyperpolarization contain the entire S4 helix of HCN1, which is unusually long in comparison with the S4 segments of depolarization-activated channels (19, 20, 41). spHCN, a sea urchin homolog, lacks four residues in this extended region of the S4 (Fig. 5*A*). Using the HEHE*H as a base construct, we examined the effect of deletions of the C-terminal end of the S4 segment. Eliminating four residues in the S4–S5 linker results in a channel that retains activation upon hyperpolarization with only minor differences compared with the parent construct (Fig. 5*B*). In contrast, removal of eight residues, which corresponds to the extra helical length of the HCN S4, results in a channel that is activated on hyperpolarization but also shows evidence of voltage-dependent inactivation beyond −100 mV (Fig. 5 *B* and *C*). Additionally, this mutant is unable to fully close, with roughly 40% of the peak conductance remaining at depolarizing potentials. These results demonstrate that neither the extra length of the HCN1 S4 nor its residue-specific interactions with the C linker are essential for activation by hyperpolarization. The longer S4 may, however, help stabilize the hyperpolarization-dependent open state and protect the channel from a voltage-dependent inactivation. Additionally, given the significant basal conductance, it may be important in stabilizing the closed state at depolarized potentials.

## Discussion

In this study, we utilized a hierarchical approach to determine how various structural elements act in concert to control the gating polarity in voltage-activated ion channels. Our primary finding is that the HCN voltage-sensing domain is able to drive voltage-dependent channel opening in both directions when coupled to the pore domain of a depolarization-activated channel. This ability to act as a bipolar switch is unique to the HCN voltage sensor, in contrast to depolarization-activated channels. This finding is incompatible with the "inverse coupling" hypothesis of HCN gating (13, 42), which assumes that the voltage sensor of HCN relies on the same conformational change as depolarization-activated channels but that the coupling between voltage sensor and pore is reversed. Therefore, these channels open when the voltage sensor is at rest. Our bipolar chimeras

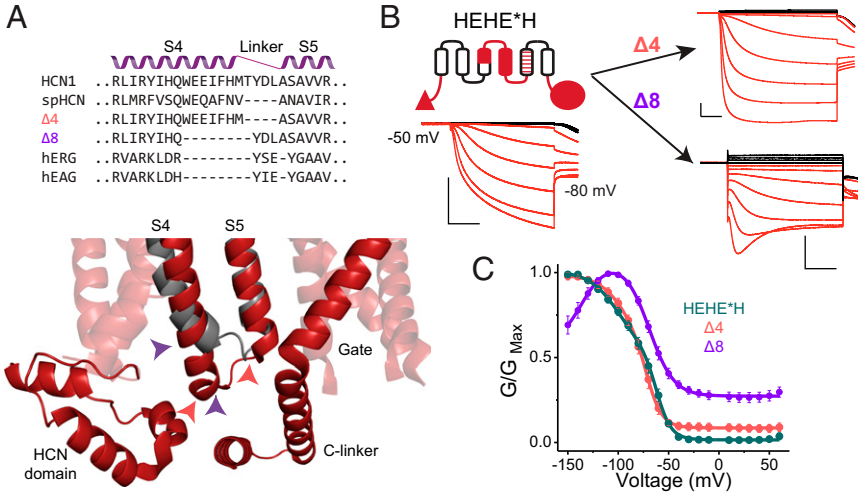


**Fig. 5.** Extra length of the S4 helix is not essential for activation by hyperpolarization. (*A*, *Top*) Sequence alignments for some HCN- and EAG-like channels in the S4–S5 helix-turn-helix region. The resulting sequences of the S4 deletion mutants generated in the background of the HEHE*H construct (Δ4 and Δ8) are also indicated. (*A*, *Bottom*) HCN1 structure in the vicinity of the S4–S5 turn of HCN1 (red) is overlaid with that of EAG1 (gray). Note the extended length of the HCN1 S4 and its close proximity to the HCN domain and C linker, suggesting a potential for functionally critical interactions. Colored arrowheads indicate deletion boundaries in Δ4 (pink) and Δ8 (purple) mutants. (*B*) Representative COVG current traces for the HEHE*H construct and its two deletion derivatives. [Scale bars, 2 μA (vertical) and 500 ms (horizontal).] (*C*) G-V curves for the parent HEHE*H and deletion mutants, with error bars representing SEM for $n = 4$.

show that the hyperpolarization- and depolarization-activation pathways are not mutually exclusive. Thus, the voltage-sensing domain of HCN channels must undergo a secondary conformational change to open the pore upon hyperpolarization. Consistent with this notion of a distinct S4 conformation, cysteine accessibility studies show that the S4 of HCN channels undergoes very little vertical displacement during channel opening (17, 18), unlike canonical depolarization-activated S4s (43–46). Remarkably, Sanguinetti and coworkers were able to identify a single-point mutation that confers the bipolar gating phenotype on hERG potassium channels (47). Thus, in wild-type depolarization-activated channels, this second transition either occurs outside the physiological voltage range or the channels lack the machinery needed to couple this transition to pore opening. Nevertheless, given the phylogenetic relationship between the hERG, EAG, and HCN channels, it appears that the bipolar gating phenotype is latent in this clade of voltage-gated ion channels.

Taking into consideration the bipolar nature of the HCN voltage sensor, we extend the canonical gating scheme to include a hyperpolarization-dependent open state ($O_H$). However, this scheme raises the following conundrum: If the HCN voltage sensor can open the pore gates in both directions, why do HCN channels open only upon hyperpolarization? We find that several other structural elements in the HCN channel act synergistically to destabilize the depolarization-activation pathway and favor hyperpolarization-dependent activation (Fig. 6*A*). Our data show that the tight interface between S4 and S5 induces the channels to rapidly enter into an inactivated state, thereby obscuring opening upon depolarization ($O_D$). The C terminus, which includes the C linker and the CNBD, plays a crucial role by destabilizing $O_D$ and favoring the hyperpolarization-dependent open state. Additionally, specific residues in the vicinity of the pore gate strongly destabilize the $O_D$ and primarily favor opening upon hyperpolarization. These terminal pore residues act independent of the C-terminal cytoplasmic domain, because the wild-type channels lacking the C terminus do not open upon depolarization (36).

To evaluate whether such a simple gating scheme can account for the full spectrum of channel properties observed in this study, we carried out kinetic simulations for an array of phenotypically diverse chimeras and mosaics (Fig. 6 *B–D*). The results of these simulations show that our unified model can in fact recapitulate not only the steady state but also the kinetic features of each construct tested here. Further, the quantitative impact of each structural element in the gating model agrees with their proposed contributions to channel activation. Our extended gating scheme is also the most parsimonious, because we have electrophysiological evidence for each of the proposed states. This model is also capable of fitting the bulk of kinetic and steady-state properties of the HCN1 and EAG parents (*SI Appendix*, Fig. S7).

Given the strikingly long S4 helix and its close apposition to the S6 helix and cytoplasmic domains in the HCN1 structure, Lee and MacKinnon (19) posited that the extra length of the

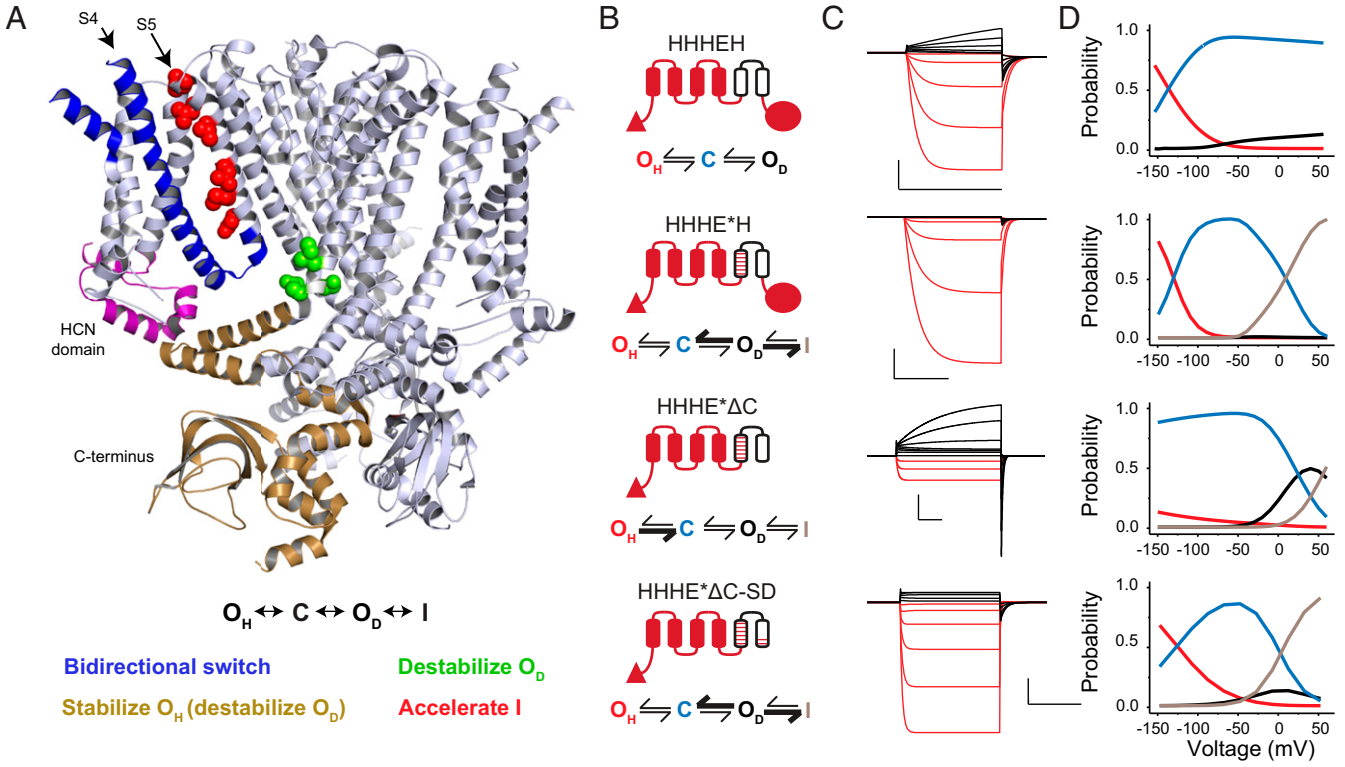


**Fig. 6.** Voltage gating scheme for the CNBD family of channels. (*A*, *Top*) A unified state model for the CNBD family of ion channels. (*A*, *Middle*) A structural map highlighting the key elements involved in determining gating polarity in HCN1 channels. Only three out of four monomers are shown for clarity. The structural elements are colored according to their influence on each of the states shown in the unified gating model. The color scheme depicting which states are stabilized or destabilized by a particular element is shown below the structure. (*B*) Cartoon representations and models for several selected chimeras and mosaics. Bolded arrows indicate transitions that are favored by introduction of the HCN-like S4–S5 interface (HHHE*H), removal of the C terminus (HHHE*ΔC), or pore mutations near the gate (HHHE*ΔC-SD). (*C*) Simulated current traces from the model in response to the same pulse protocol applied in the electrophysiological recordings for each construct. Parameters for simulations can be found in *SI Appendix*, Table S1. (*D*) Probability vs. voltage curves for each state in the model measured as the probability of occupancy of each state over the final 10 ms of each test pulse. Probability curves for the hyperpolarized open state are colored red, the closed state is in blue, depolarized open state is in black, and inactivated state is in gray.

HCN1 voltage sensor is the "key" determinant for hyperpolarization activation. Consistent with this notion, deletions of stretches of three residues from the S4 helix of the spHCN channel result in a loss of activation upon hyperpolarization (48). Remarkably, we find that truncating the S4 of hHCN1 by as much as three helical turns, matching the length of the EAG S4, does not eliminate activation upon hyperpolarization, although it increases the basal leak through these channels. While these contrasting findings are difficult to reconcile and further studies are warranted, we note that the cyclic nucleotides profoundly modulate channel opening upon hyperpolarization in spHCN channels, unlike their mammalian counterparts. Therefore, it is possible that a shortened S4 helix of spHCN is not able to overcome the strong modulatory effect of the CNBD. Nevertheless, our data are clear that the extra length of the S4 is not a critical determinant for the opening of mammalian HCN channels.

Our findings naturally raise the question that if it is not the unique length of the S4 helix, then what enables the HCN voltage sensor to act as a "bipolar switch"? While further studies are required to probe the underlying mechanisms, we note that in all of the hyperpolarization-activated channels, a conserved hydrophobic residue in the middle of the S4 helix is replaced by a serine. Given the propensity of serines to act as helix breakers (49), we speculate that a bending or twisting motion originating at these sites may relieve inhibition on the pore domain (48), allowing these channels to open on hyperpolarization.

Finally, in addition to identifying the essential molecular mechanisms of hyperpolarization gating, our studies provide a unifying framework for understanding how channels with a common architecture give rise to the whole spectrum of voltage-dependent phenotypes observed in the VGIC superfamily. In addition, given that our chimeras and mosaics stabilize the channel in different states, they may serve as good models for further structural and mechanistic analyses of electromechanical coupling in hyperpolarization-activated channels.

## Materials and Methods

**Alignments.** Structural alignments were carried out by PyMOL 1.8 (50) using the default settings from the "super" command. Sequences for hHCN1 (UniProt ID code O60741), mHCN2 (O88703), spHCN (O76977), LKT1 (Q9LEG6), KAT1 (Q39128), SKOR (Q9M8S6), rEAG1 (Q63472), and hERG (Q12809) were first aligned by T-Coffee Expresso (51) and then manually adjusted based on structural alignments.

**Molecular Biology.** Chimeras between mHCN1 [National Center for Biotechnology Information (NCBI) accession no. NM_010408.3] and hEAG1 (NM_172362.2) were generated in the pUNIV vector (52) as fusions with the *Xenopus laevis* codon-optimized gene for mCherry at the 3′ end. Chimeragenesis was done by a QuikChange cloning protocol that involves performing a standard QuikChange mutagenesis reaction in which a PCR-synthesized fragment of interest with terminal arms that anneal to the target plasmid is used in place of mutagenic oligonucleotides. The conditions and reagents used were exactly as previously described (53). The HCN1 C terminus was deleted following residue A624, analogous to the deletion in hHCN1 used previously in structure determination (19). Mosaic mutations were similarly introduced by QuikChange cloning using the gBlock DNA fragment (Integrated DNA Technologies). Point mutations were introduced by a QuikChange protocol using high-fidelity PfuUltra II Fusion polymerase (Agilent) and a single mutagenic primer in the reaction. In all cases, the sequence of the entire ORF was verified by Sanger sequencing of both DNA strands. Chimeras with spHCN (NCBI accession no. NM_214564.1) or mHCN2 (NM_008226.2) were generated in the psGEM vector.

**Recombinant Expression and Electrophysiology.** Procedures were performed in accordance with Institutional Animal Care and Use Committee (IACUC) protocols and approved by the School of Medicine and Public Health Animal Care and Use Committee at the University of Wisconsin-Madison. Oocytes from *X. laevis* were isolated via surgery and digested using 0.8 mg/mL collagenase II (Roche) for ∼1 h until the removal of the follicular layer. Oocytes were maintained in ND96 solution (96 mM NaCl, 2 mM KCl, 1 mM $CaCl_2$, 1 mM $MgCl_2$, 5 mM Hepes, pH 7.4) before injection and then transferred to ND96 containing antibiotics (50 μg/mL gentamicin and ciprofloxacin, 100 μg/mL tetracycline, penicillin, and streptomycin) and BSA (0.5 mg/mL) after injections. Oocytes were microinjected with 20 to 70 nL corresponding to 5 to 75 ng cRNA using a Nanoject II (Drummond Scientific). Injections were performed in ND96 solution without calcium chloride, and then oocytes were transferred to the postinjection solution described above.

Cut-open Vaseline gap (COVG) voltage-clamp recordings were obtained at room temperature (22 °C) with a CA-1B amplifier (Dagan) at a sampling rate of 10 kHz. Two-electrode voltage-clamp (TEVC) recordings were obtained at room temperature with an OC-725C amplifier (Warner) at a sampling rate of 10 kHz. Thin-walled glass pipettes (World Precision Instruments) were used with tip resistances of 0.2 to 0.8 MΩ and filled with 3 M KCl. Unless otherwise noted, external solutions contained 100 mM KOH, 5 mM NaOH, 20 mM Hepes, and 2 mM $CaCl_2$. Internal solutions were composed of 100 mM KOH, 5 mM NaOH, 10 mM Hepes, and 2 mM EGTA. For COVG experiments, oocytes were permeabilized using 0.3% saponin in the internal solution and washed out before recording. All solutions were adjusted to pH 7.4 using methanesulfonic acid. All recordings were obtained with no leak subtraction, though capacitance compensation was used in COVG experiments to improve resolution of constructs with fast kinetics. Currents at the end of the test pulse were converted to conductance by dividing by the potential of the test pulse (assuming a reversal potential of 0 mV due to symmetrical recording solutions). This assumes that the changes in the maximum conductance are due to changes in open probabilities rather than single-channel conductances. Due to the inability to determine conductance at 0 mV in symmetrical solutions, this point is omitted from all conductance–voltage (G-V) curves. Conductance at the peak tail was determined by dividing the peak tail current amplitude by the potential at the tail pulse (generally −80 mV). Data in G-V curves were fitted to a sum of two Boltzmann curves in Origin 2017 (OriginLab) with the function $f(x) = O_1 + (A_1 - O_2)/(1 + \exp(k_1(V - V_1))) + O_2 + (A_2 - O_2)/(1 + \exp(k_2(V - V_2)))$, where $A_1$ and $A_2$ represent the amplitudes, $O_1$ and $O_2$ represent the offsets, $V_1$ and $V_2$ represent $V_{1/2}$, and $k_1$ and $k_2$ represent the slope factors for two independent components. As many curves do not reach saturation, curves are primarily provided for visual reference.

**MTSEA Modification Experiments.** MTSEA modification was assessed by TEVC. Oocytes were perfused with external solution and given repeated test pulses every 30 s. Perfusion was halted before a test pulse to avoid additional noise in the recording. When recordings stabilized, perfusion was switched to external solution containing 5 mM MTSEA, and pulses continued. This solution was prepared fresh for each oocyte from a 1 M stock of MTSEA dissolved in external solution and kept on ice, which was prepared daily.

**Model Simulations.** Kinetic models were built and simulated using the software Kinetic Model Builder version 2.0 described previously (54). All rates were allowed to vary between 0 and 1,000 $s^{-1}$, while charge was limited to 0 to 3 $e^{-}$. Initial values for the rate and charge of each step were set to 1, and then current traces were fit using the EigenSolver mode of the Kinetic Model Builder software until convergence. Weighting was used to better recapitulate the kinetics of the process and avoid the bias of overfitting the steady state. This was accomplished by weighting the fit immediately following the test and tail pulse 10-fold compared with the steady state. This weight decayed exponentially back to baseline with a time constant of 10 ms using the built-in capabilities of the software. State probability at "steady state" was determined by the occupancy of each state in the model over the last 10 ms of the test pulse. Briefly, the state occupancy was determined by numerical solution of the transition matrices within the model as described previously (54, 55).

**Quantitative and Statistical Analysis.** Clampfit (Molecular Devices) was used to quantitate currents at steady state. Origin was used to fit data points to a sum of two Boltzmann curves. Kinetic Model Builder was used for all kinetic simulations. PyMOL was used for all structural analyses. Throughout the paper, *n* is used to denote the number of oocytes tested in each experiment as indicated in each figure legend.

**ACKNOWLEDGMENTS.** We thank G. A. Robertson for providing hEAG1, C. Czajkowski for the pUNIV vector, B. Santoro and S. A. Siegelbaum for mHCN1, M. C. Sanguinetti for mHCN2, and U. B. Kaupp for spHCN. We also thank N. Nallappan for help generating chimeras; N. Nallappan, W. Stevens-Sostre, and T. Tsao for performing frog surgeries and providing oocytes; and M. B. Jackson, L. Delemotte, and G. A. Robertson for their helpful comments and discussions.

We thank M. Kasimova and L. Delemotte for sharing unpublished results of their molecular dynamics simulations. This work was supported by funding from the National Institutes of Health to B.C. (Grant NS101723), J.C. (Award T32 HL-07936-17), and C.A.-B. (Award T32 HL-07936-15), American Heart Association to C.A.-B. (Award 17POST33411069), Romnes faculty fellowship (to B.C.), and Hilldale fellowships (to A.B.).

1. Bezanilla F (2000) The voltage sensor in voltage-dependent ion channels. *Physiol Rev* 80:555–592.
2. Hodgkin AL, Huxley AF (1952) Currents carried by sodium and potassium ions through the membrane of the giant axon of *Loligo*. *J Physiol* 116:449–472.
3. Ludwig A, Zong X, Jeglitsch M, Hofmann F, Biel M (1998) A family of hyperpolarization-activated mammalian cation channels. *Nature* 393:587–591.
4. Santoro B, et al. (1998) Identification of a gene encoding a hyperpolarization-activated pacemaker channel of brain. *Cell* 93:717–729.
5. Brown HF, DiFrancesco D, Noble SJ (1979) How does adrenaline accelerate the heart? *Nature* 280:235–236.
6. Yu FH, Yarov-Yarovoy V, Gutman GA, Catterall WA (2005) Overview of molecular relationships in the voltage-gated ion channel superfamily. *Pharmacol Rev* 57: 387–395.
7. Craven KB, Zagotta WN (2006) CNG and HCN channels: Two peas, one pod. *Annu Rev Physiol* 68:375–401.
8. James ZM, Zagotta WN (2018) Structural insights into the mechanisms of CNBD channel function. *J Gen Physiol* 150:225–244.
9. Sanguinetti MC, Jiang C, Curran ME, Keating MT (1995) A mechanistic link between an inherited and an acquired cardiac arrhythmia: HERG encodes the IKr potassium channel. *Cell* 81:299–307.
10. Vandenberg JI, Perozo E, Allen TW (2017) Towards a structural view of drug binding to hERG $K^+$ channels. *Trends Pharmacol Sci* 38:899–907.
11. Trudeau MC, Warmke JW, Ganetzky B, Robertson GA (1995) HERG, a human inward rectifier in the voltage-gated potassium channel family. *Science* 269:92–95.
12. Smith PL, Baukrowitz T, Yellen G (1996) The inward rectification mechanism of the HERG cardiac potassium channel. *Nature* 379:833–836.
13. Männikkö R, Elinder F, Larsson HP (2002) Voltage-sensing mechanism is conserved among ion channels gated by opposite voltages. *Nature* 419:837–841.
14. Rothberg BS, Shin KS, Phale PS, Yellen G (2002) Voltage-controlled gating at the intracellular entrance to a hyperpolarization-activated cation channel. *J Gen Physiol* 119:83–91.
15. Rothberg BS, Shin KS, Yellen G (2003) Movements near the gate of a hyperpolarization-activated cation channel. *J Gen Physiol* 122:501–510.
16. Shin KS, Rothberg BS, Yellen G (2001) Blocker state dependence and trapping in hyperpolarization-activated cation channels: Evidence for an intracellular activation gate. *J Gen Physiol* 117:91–101.
17. Bell DC, Yao H, Saenger RC, Riley JH, Siegelbaum SA (2004) Changes in local S4 environment provide a voltage-sensing mechanism for mammalian hyperpolarization-activated HCN channels. *J Gen Physiol* 123:5–19.
18. Vemana S, Pandey S, Larsson HP (2004) S4 movement in a mammalian HCN channel. *J Gen Physiol* 123:21–32.
19. Lee CH, MacKinnon R (2017) Structures of the human HCN1 hyperpolarization-activated channel. *Cell* 168:111–120.e11.
20. Whicher JR, MacKinnon R (2016) Structure of the voltage-gated $K^+$ channel Eag1 reveals an alternative voltage sensing mechanism. *Science* 353:664–669.
21. Morais Cabral JH, et al. (1998) Crystal structure and functional analysis of the HERG potassium channel N terminus: A eukaryotic PAS domain. *Cell* 95:649–655.
22. Haitin Y, Carlson AE, Zagotta WN (2013) The structural mechanism of KCNH-channel regulation by the eag domain. *Nature* 501:444–448.
23. Lu Z, Klem AM, Ramu Y (2001) Ion conduction pore is conserved among potassium channels. *Nature* 413:809–813.
24. Lu Z, Klem AM, Ramu Y (2002) Coupling between voltage sensors and activation gate in voltage-gated $K^+$ channels. *J Gen Physiol* 120:663–676.
25. Alabi AA, Bahamonde MI, Jung HJ, Kim JI, Swartz KJ (2007) Portability of paddle motif function and pharmacology in voltage sensors. *Nature* 450:370–375.
26. Arrigoni C, et al. (2013) The voltage-sensing domain of a phosphatase gates the pore of a potassium channel. *J Gen Physiol* 141:389–395.
27. Hausdorff SF, Goldstein SAN, Rushin EE, Miller C (1991) Functional characterization of a minimal $K^+$ channel expressed from a synthetic gene. *Biochemistry* 30:3341–3346.
28. Starace DM, Bezanilla F (2004) A proton pore in a potassium channel voltage sensor reveals a focused electric field. *Nature* 427:548–553.
29. Starace DM, Stefani E, Bezanilla F (1997) Voltage-dependent proton transport by the voltage sensor of the Shaker $K^+$ channel. *Neuron* 19:1319–1327.
30. Tombola F, Pathak MM, Isacoff EY (2005) Voltage-sensing arginines in a potassium channel permeate and occlude cation-selective pores. *Neuron* 45:379–388.
31. Long SB, Campbell EB, Mackinnon R (2005) Voltage sensor of Kv1.2: Structural basis of electromechanical coupling. *Science* 309:903–908.
32. Shin KS, Maertens C, Proenza C, Rothberg BS, Yellen G (2004) Inactivation in HCN channels results from reclosure of the activation gate: Desensitization to voltage. *Neuron* 41:737–744.
33. Carlson AE, Brelidze TI, Zagotta WN (2013) Flavonoid regulation of EAG1 channels. *J Gen Physiol* 141:347–358.
34. Terlau H, Heinemann SH, Stühmer W, Pongs O, Ludwig J (1997) Amino terminal-dependent gating of the potassium channel rat eag is compensated by a mutation in the S4 segment. *J Physiol* 502:537–543.
35. Lin TF, et al. (2014) The Eag domain regulates the voltage-dependent inactivation of rat Eag1 $K^+$ channels. *PLoS One* 9:e110423.
36. Wainger BJ, DeGennaro M, Santoro B, Siegelbaum SA, Tibbs GR (2001) Molecular mechanism of cAMP modulation of HCN pacemaker channels. *Nature* 411:805–810.
37. Rheinberger J, Gao X, Schmidpeter PAM, Nimigean CM (2018) Ligand discrimination and gating in cyclic nucleotide-gated ion channels from apo and partial agonist-bound cryo-EM structures. *eLife* 7:e39775.
38. Wang J, Chen S, Siegelbaum SA (2001) Regulation of hyperpolarization-activated HCN channel gating and cAMP modulation due to interactions of COOH terminus and core transmembrane regions. *J Gen Physiol* 118:237–250.
39. Zagotta WN, et al. (2003) Structural basis for modulation and agonist specificity of HCN pacemaker channels. *Nature* 425:200–205.
40. Decher N, Chen J, Sanguinetti MC (2004) Voltage-dependent gating of hyperpolarization-activated, cyclic nucleotide-gated pacemaker channels: Molecular coupling between the S4-S5 and C-linkers. *J Biol Chem* 279:13859–13865.
41. Wang W, MacKinnon R (2017) Cryo-EM structure of the open human ether-à-go-go-related $K^+$ channel hERG. *Cell* 169:422–430.e10.
42. Latorre R, et al. (2003) Molecular coupling between voltage sensor and pore opening in the *Arabidopsis* inward rectifier $K^+$ channel KAT1. *J Gen Physiol* 122:459–469.
43. Ahern CA, Horn R (2005) Focused electric field across the voltage sensor of potassium channels. *Neuron* 48:25–29.
44. Chanda B, Asamoah OK, Blunck R, Roux B, Bezanilla F (2005) Gating charge displacement in voltage-gated ion channels involves limited transmembrane movement. *Nature* 436:852–856.
45. Larsson HP, Baker OS, Dhillon DS, Isacoff EY (1996) Transmembrane movement of the Shaker $K^+$ channel S4. *Neuron* 16:387–397.
46. Starace DM, Bezanilla F (2001) Histidine scanning mutagenesis of basic residues of the S4 segment of the Shaker $K^+$ channel. *J Gen Physiol* 117:469–490.
47. Tristani-Firouzi M, Chen J, Sanguinetti MC (2002) Interactions between S4-S5 linker and S6 transmembrane domain modulate gating of HERG $K^+$ channels. *J Biol Chem* 277:18994–19000.
48. Flynn GE, Zagotta WN (2018) Insights into the molecular mechanism for hyperpolarization-dependent activation of HCN channels. *Proc Natl Acad Sci USA* 115:E8086–E8095.
49. Ballesteros JA, Deupi X, Olivella M, Haaksma EEJ, Pardo L (2000) Serine and threonine residues bend alpha-helices in the chi(1) = g(-) conformation. *Biophys J* 79:2754–2760.
50. Schrodinger, LLC (2015) The PyMOL Molecular Graphics System (Schrodinger, New York), Version 1.8.
51. Notredame C, Higgins DG, Heringa J (2000) T-Coffee: A novel method for fast and accurate multiple sequence alignment. *J Mol Biol* 302:205–217.
52. Venkatachalan SP, et al. (2007) Optimized expression vector for ion channel studies in *Xenopus* oocytes and mammalian cells using alfalfa mosaic virus. *Pflugers Arch* 454:155–163.
53. Klenchin VA, Frye JJ, Jones MH, Winey M, Rayment I (2011) Structure-function analysis of the C-terminal domain of CNM67, a core component of the *Saccharomyces cerevisiae* spindle pole body. *J Biol Chem* 286:18240–18250.
54. Goldschen-Ohm MP, Haroldson A, Jones MV, Pearce RA (2014) A nonequilibrium binary elements-based kinetic model for benzodiazepine regulation of GABAA receptors. *J Gen Physiol* 144:27–39.
55. Colquhoun D, Hawkes AG (1995) A Q-matrix cookbook: How to write only one program to calculate the single-channel and macroscopic predictions for any kinetic mechanism. *Single-Channel Recordings*, eds Sakmann B, Neher E (Plenum, New York), pp 589–633.